催化学报
2011 Chinese Journal of Catalysis Vol. 32 No. 6

文章编号: 0253-9837(2011)06-0939-11 国际版 DOI: 10.1016/S1872-2067(10)60215-X 研究论文: 939~949

单斜$BiVO_4$可见光催化降解甲基橙的形貌效应

蒋海燕, 戴洪兴*, 孟 雪, 张 磊, 邓积光, 吉科猛

北京工业大学环境与能源工程学院化学化工系, 北京 100124

摘要: 以硝酸铋和偏钒酸铵为无机源, NaOH 为 pH 值调节剂, 三嵌段共聚物 P123 为表面活性剂, 采用醇-水热法制备了多种形貌的单斜 $BiVO_4$. 利用 X 射线衍射、N_2 吸脱附、扫描电子显微镜、X 射线光电子能谱和紫外可见光漫反射等技术表征了其物化性质, 并考察了这些 $BiVO_4$ 样品在可见光照射下降解甲基橙的催化活性. 结果表明, 表面活性剂和溶液 pH 值对所得 $BiVO_4$ 产物的粒子形貌影响很大. 在醇-水热温度为 180 °C, pH 值为 2, 7 或 10 时, 可分别制得多孔球状、花状和片状 $BiVO_4$; 而采用 P123 作表面活性剂, 在醇-水热温度为 180 °C 且 pH 为 2 时可制得棒状 $BiVO_4$. $BiVO_4$ 样品粒子形貌的不同导致它们的比表面积、表面氧空位密度和 (040) 晶面暴露率不同, 其中以棒状 $BiVO_4$ 样品具有最高的比表面积、氧空位密度和 (040) 晶面暴露率以及最低的带隙能, 使其对甲基橙降解表现出最好的光催化活性. 可以认为, $BiVO_4$ 样品对甲基橙的光催化降解反应活性存在形貌效应, 棒状形貌有利于提高 $BiVO_4$ 的光催化性能.

关键词: 醇-水热法; 形貌相依性质; 可见光响应催化剂; 单斜钒酸铋; 甲基橙; 降解

中图分类号: O643 **文献标识码:** A

收稿日期: 2011-01-11. 接受日期: 2011-02-28.

*通讯联系人. 电话: (010)67396118; 传真: (010)67391983; 电子信箱: hxdai@bjut.edu.cn

基金来源: 国家自然科学基金 (20973017, 21077007); 国家高技术研究发展计划 (863 计划, 2009AA063201); 服务北京创新人才项目 (00500054R4003); 北京市教委创新团队项目 (PHR200907105, PHR201007105)

本文的英文电子版(国际版)由Elsevier出版社在ScienceDirect上出版(http://www.sciencedirect.com/science/journal/18722067).

Morphology-Dependent Photocatalytic Performance of Monoclinic $BiVO_4$ for Methyl Orange Degradation under Visible-Light Irradiation

JIANG Haiyan, DAI Hongxing*, MENG Xue, ZHANG Lei, DENG Jiguang, JI Kemeng

Department of Chemistry and Chemical Engineering, College of Environmental and Energy Engineering, Beijing University of Technology, Beijing 100124, China

Abstract: Monoclinic $BiVO_4$ with multiple morphologies were fabricated using the alcoho-hydrothermal strategy with bismuth nitrate and ammonium metavanadate as inorganic sources, NaOH for pH adjustment, and the triblock copolymer P123 as a surfactant. The materials were characterized by X-ray diffraction, nitrogen adsorption-desorption, scanning electron microscopy, X-ray photoelectron spectroscopy, and ultraviolet-visible diffuse reflectance spectroscopy. The photocatalytic performance of the $BiVO_4$ samples was evaluated for the degradation of methyl orange (MO) under visible-light irradiation condition. The results showed that the surfactant and pH had a significant influence on the particle morphology of the $BiVO_4$ product. Porous spherical, flower-like, and sheet-like $BiVO_4$ were fabricated at an alcoho-hydrothermal temperature of 180 °C and at a pH of 2, 7, or 10, respectively, whereas rod-like $BiVO_4$ was obtained in the presence of P123 at an alcoho-hydrothermal temperature of 180 °C and at a pH of 2. The difference in $BiVO_4$ particle morphology led to differences in surface area, surface oxygen vacancy density, and (040) crystal plane exposure. Among the four $BiVO_4$ samples, the rod-like sample had the highest surface area, surface oxygen vacancy density, and (040) crystal plane exposure, and the lowest bandgap energy resulting in it having the best photocatalytic activity for MO photodegradation. It can be concluded that a morphological effect is responsible for the photocatalytic performance and the rod-like morphology seems to favor an enhancement in the photocatalytic performance of the $BiVO_4$ material.

Key words: alcoho-hydrothermal strategy; morphology-dependent property; visible-light-driven catalyst; monoclinic bismuth vanadate; methyl orange; degradation

Received 11 January 2011. Accepted 28 February 2011.
**Corresponding author. Tel: +98-10-67396118; Fax: +98-10-67391983; E-mail: hxdai@bjut.edu.cn*
This work was supported by the National Natural Science Foundation of China (20973017 and 21077007), the National High Technology Research and Development Program of China (863 Program, 2009AA063201), the Creative Research Foundation of Beijing University of Technology (00500054R4003), and the Creative Research Team of Beijing Municipal Commission of Education of Education (PHR200907105, PHR201007105).
English edition available online at Elsevier ScienceDirect (http://www.sciencedirect.com/science/journal/18722067).

近年来, $BiVO_4$ 因其独特的物化性质, 如铁弹性[1]、离子导电性[2]和可见光响应的光催化活性[3,4]而备受关注. $BiVO_4$ 存在四方锆石型、单斜白钨矿型和四方白钨矿型3种晶相结构, 其中以单斜相 $BiVO_4$ 的可见光催化活性更高[5]. 众所周知, 样品晶体结构与其制备方法有关. 四方相 $BiVO_4$ 通常在低温下通过沉淀法制得, 而单斜相 $BiVO_4$ 制备则有多种方法, 如固相合成法[6], 共沉淀法[7], 溶剂热或水热法[3,4], 化学浴沉积法[8], 金属有机物分解法[9]和超声化学法[10]. 其中, 溶剂热或水热法是一种制备具有完美晶相结构和规则形貌的单斜相 $BiVO_4$ 的有效且环保方法[11]. 迄今为止, 大量具有不同形貌的单斜相 $BiVO_4$ 可通过溶剂热或水热法合成. 例如, 采用溶剂热法在150 °C处理 $Bi(NO_3)_3$ 和 $NaVO_4$ 的混合物可制得单斜相 $BiVO_4$ 纺锤状微米管[3]. Sun等[12]以水和乙醇的混合液为溶剂, 乙二胺四乙酸为络合剂, 采用水热法合成出了由纳米片堆积而成的星状单斜相 $BiVO_4$. Zhang等[13]以 $Bi(NO_3)_3$ 和 NH_4VO_3 为原料, 十二烷基苯磺酸钠为结构导向剂, 制得了单斜相 $BiVO_4$ 纳米片. 大量研究表明, 微纳米无机材料存在形貌效应. 例如, ZnO形貌不同, 其催化活性也不一样, 在*N*-甲酰化反应中, 具有大量极性晶面的ZnO具有更高的催化活性[14]. 在光催化降解亚甲基蓝的反应中, 沿(0001)轴生长的六方片状ZnO纳米晶表现出5倍于棒状ZnO粒子的催化活性[15]. 然而, 迄今为止, 有关可见光响应型 $BiVO_4$ 的形貌效应的报道较少. Xi等[16]在进行可见光催化降解罗丹明B (RhB)和光催化氧化水释 O_2 反应时发现, 表面暴露(001)晶面的 $BiVO_4$ 纳米片具有好的催化活性. Zhang等[13]观察到具有(010)晶面优先取向的 $BiVO_4$ 纳米片在太阳光照射下对RhB的降解显示良好的催化活性. Wang等[17]发现在光催化氧化水释 O_2 反应中, 具有优先暴露(040)晶面的 $BiVO_4$ 微米片具有优异的催化活性.

近年来, 大量的 $BiVO_4$ 基材料已用作降解有机物(亚甲基蓝(MB)[18], RhB[13], 甲基橙(MO)[19]和甲苯[20])的光催化剂. 最近, 本课题组研究了规整形貌的单晶 $BiVO_4$ 的可控制备及其可见光催化性能, 发现这些单晶材料在光催化降解MB的反应中具有良好的光催化活性[21]. 作为该项工作的延续, 本文采用醇-水热法合成不同粒子形貌的单斜相 $BiVO_4$, 并研究了它们的光催化性能.

1 实验部分

1.1 $BiVO_4$ 样品的制备

以 $Bi(NO_3)_3·5H_2O$ 和 NH_4VO_3 为无机源, 水和乙醇混合物为溶剂, 在有或无表面活性剂P123条件下, 采用醇-水热法制备了不同粒子形貌的 $BiVO_4$ 样品, 具体步骤如下. 将10 mmol研磨好的 $Bi(NO_3)_3·5H_2O$ 或1.972 g P123 (Bi/P123摩尔比 = 1:0.034)加入到5 ml硝酸(67%)和50 ml无水乙醇的混合液中. 充分搅拌后, 再加入10 mmol研磨好的 NH_4VO_3 粉末, 用饱和NaOH的乙醇溶液调节体系的pH值至2, 7或10. 将80 ml上述混合溶液转移至100 ml自压釜内(如混合液体积不足80 ml, 则以无水乙醇补充), 在180 °C经醇-水热处理12 h. 将所得黄色前驱物过滤, 洗涤3次, 于60 °C干燥12 h, 再在马弗炉中以1 °C/min从室温升至400 °C并保持4 h, 得到 $BiVO_4$ 样品. 在不加P123及pH = 2, 7或10条件下得到的样品分别记为 $BiVO_4$-1, $BiVO_4$-2和 $BiVO_4$-3. 在加入P123及pH = 2的条件下得到的样品记为 $BiVO_4$-4.

1.2 $BiVO_4$ 样品的表征

利用Bruker D8 Advance型X射线衍射(XRD)仪(40 kV, 35 mA)测定样品的晶相结构, Cu靶, Ni滤光片(λ = 0.15406 nm). 利用比表面仪(Micromeritics ASAP 2020)通过 N_2 在−196 °C的吸附测定样品的比表面积, 在测定前样品预先在250 °C脱气3 h, 采用BET法计算比表面积. 利用扫描电子显微镜(SEM, Zeiss Supra 55)观察样品粒子的形貌, 工作电压10 kV.

利用X射线光电子能谱(XPS, VG CLAM 4 MCD)仪分别测定样品表面Bi, V和O物种的Bi 4*f*, V 2*p*和O 1*s*的结合能(E_b); Mg K_α ($h\nu$ = 1253.6 eV)为激发源. 测定前将样品用20 ml/min的O_2于400 °C处理1 h, 待其在充有He的手套箱(研究与工业仪器公司, USA)中冷却至室温后, 再在He气氛下将它转移至光谱仪中, 在分析室分析该样品之前, 先在制备室中抽气0.5 h. 用284.6 eV的C 1*s*来校对结合能. 利用紫外-可见光漫反射光谱仪(UV-Vis DRS, UV-2450)测定样品的吸光性质, 以$BaSO_4$为参比.

1.3 $BiVO_4$样品的评价

在可见光照射下, $BiVO_4$样品降解MO反应在石英反应器(QO250, 北京畅拓科技有限公司)上进行. 光源为300 W Xe灯, 与反应器相隔5 cm. 使用400 nm滤光片确保反应时光源为可见光(λ > 400 nm). 将0.1 g $BiVO_4$样品分散于100 ml MO溶液(初始浓度c_0 = 1.0×10^{-5} mol/L)中, 超声振荡0.5 h后于暗处磁力搅拌3 h以达到吸附平衡. 以循环冷却水保持反应液温度为25 °C. 每隔30 min取样, 经离心后, 用UV-Vis仪测定反应一定时间(t)后溶液的吸光度(λ = 464 nm), 得到MO浓度(c_t), 以c_t/c_0比值来评价样品的光催化降解效率.

2 结果与讨论

2.1 样品的晶相与表面积

图1为不同条件下制得的$BiVO_4$样品的XRD谱. 可以看出, 每个样品的衍射峰均与标准单相单斜结构$BiVO_4$(JCPDS 83-1700)的一致, 无杂相, 且各样品的衍射峰强度相差不大, 说明其结晶度大致相当. 这表明改变前驱体溶液的pH值或添加表面活性剂P123对所得$BiVO_4$样品结晶度的影响较小. 还可以看出, $BiVO_4$-1, $BiVO_4$-2, $BiVO_4$-3和$BiVO_4$-4样品的(040)和(112)晶面的衍射峰强度之比分别为0.22, 0.23, 0.32和0.36, 此值越高, 表明样品的(040)晶面暴露率越高. 可见, $BiVO_4$样品(040)晶面暴露率最高. 有研究[17]表明, $BiVO_4$样品中(040)晶面的暴露量与其制备方法和粒子形貌有关, (040)晶面的优先暴露有利于提高$BiVO_4$材料的光催化活性.

表1为$BiVO_4$样品的制备条件和部分物理性质. 可以看出, 于400 °C焙烧后制得的$BiVO_4$-3和$BiVO_4$-4样品的比表面积分别为3.5和3.8 m^2/g, 高于

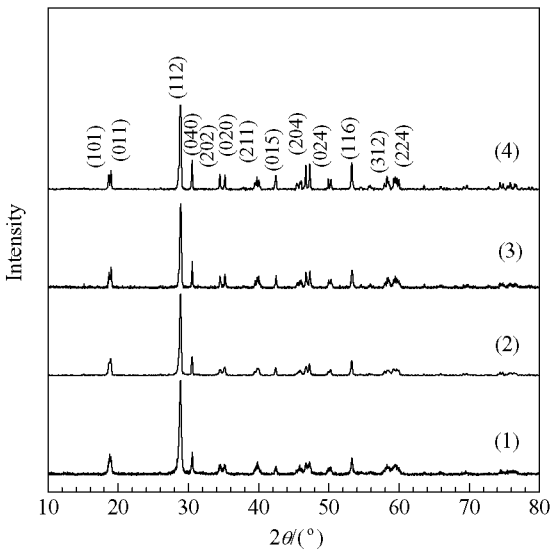

图1 各$BiVO_4$样品的XRD谱

Fig. 1. XRD patterns of different $BiVO_4$ samples. (1) $BiVO_4$-1; (2) $BiVO_4$-2; (3) $BiVO_4$-3; (4) $BiVO_4$-4. $BiVO_4$-1, $BiVO_4$-2, and $BiVO_4$-3 were prepared without using surfactant P123 at pH = 2, 7, and 10, respectively. $BiVO_4$-4 was prepared using surfactant P123 at pH = 2.

文献[22,23]报道的未焙烧$BiVO_4$的(0.3~2.2 m^2/g). 而且, $BiVO_4$-3样品的比表面积远大于$BiVO_4$-1和$BiVO_4$-2样品的. 在pH = 2时, 添加P123所制得的$BiVO_4$-4样品比表面积比不加表面活性剂所制得$BiVO_4$-1样品的更大. 由此可见, 体系的pH值和表面活性剂显著影响$BiVO_4$样品的比表面积. Zhang等[24]和本课题组[22]也发现类似现象.

表1 $BiVO_4$样品的晶相结构、粒子形貌、比表面积和带隙能(E_g)

Table 1 Crystal phases, particle morphologies, BET surface areas, and bandgap energies of the as-fabricated $BiVO_4$ samples

Sample	Crystal phase	Morphology	Surface area (m^2/g)	E_g/eV
$BiVO_4$-1	monoclinic	porous spherical	1.4	2.54
$BiVO_4$-2	monoclinic	flower-like	2.1	2.52
$BiVO_4$-3	monoclinic	sheet-like	3.5	2.48
$BiVO_4$-4	monoclinic	rod-like	3.8	2.47

E_g—Bandgap energy.

2.2 样品形貌和形成机理

图2是各$BiVO_4$样品的SEM照片. 可以看出, $BiVO_4$-1样品是由具有孔结构的球状微米粒子组成, 且每个球状粒子是由众多粒径为2~11 μm的锥形微米晶体聚结而成(见图2(a)和(b)). Li等[25]采用*N*,*N*-

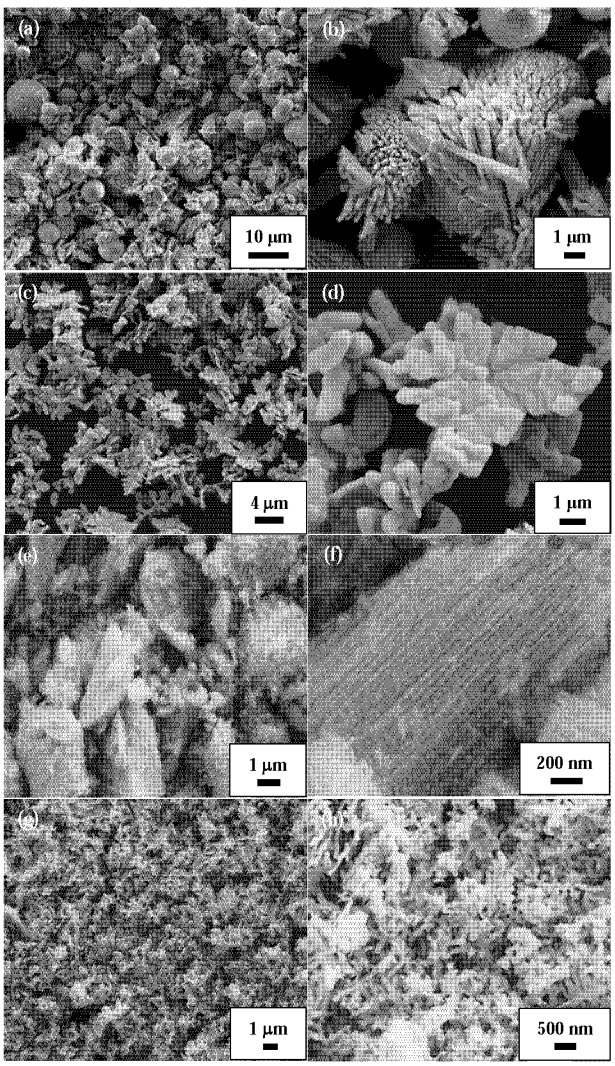

图 2 各 $BiVO_4$ 样品的 SEM 照片

Fig. 2. SEM images of $BiVO_4$-1 (a, b), $BiVO_4$-2 (c, d), $BiVO_4$-3 (e, f), and $BiVO_4$-4 (g, h) samples.

二甲基乙酰胺或 *N*-甲基-2-吡咯烷酮通过均相沉淀法制得了亚微米级的不规整的球状 $BiVO_4$. 随着前驱体溶液 pH 值由 2 升至 7 或 10, 所得 $BiVO_4$-2 和 $BiVO_4$-3 样品分别呈现花状和片状的形貌 (见图 2(c~f)). Ge 等[19]也曾制得花状 $BiVO_4$ 粒子. 当 pH=2 时, 以 P123 为表面活性剂所得的 $BiVO_4$-4 样品呈现出长为 0.5~3 μm, 直径为 100~250 nm 的棒状结构. 由此可见, 前驱体溶液的 pH 值和表面活性剂对所制备 $BiVO_4$ 材料的形貌影响很大.

众所周知, 在水热过程中, 碱源、金属源、pH 值、水热温度和水热时间均影响所制样品的粒子形貌[26]. 特定形貌微纳米晶体的形成可用定向聚集机理来解释[27], 即初级粒子优先定向自组装成高度有序的特定形貌的超结构以降低表面能. 本文中不同形貌 $BiVO_4$ 粒子的形成可能也遵循上述机理. 在加入 NaOH 的醇溶液之前, 前驱体溶液 pH 较低 (pH=0.8), 钒物种主要以 VO_3^- 形式存在[28]. 当 pH 值调节到 2, 7 或 10 时, 这些初级纳米粒子根据特定的取向能进一步自组装并经 Ostwald 熟化过程和 400 °C 焙烧后最终长成为球状, 花状或片状 $BiVO_4$ 粒子. 然而, 在 P123 存在下, 表面活性剂分子能选择性地吸附在 $BiVO_4$ 晶核表面[29], 被吸附的 P123 分子可作为捕获剂以降低所吸附晶面的生长速率从而抑制了垂直于这个轴方向的晶面的生长, 导致形成 $BiVO_4$ 微纳米棒状粒子. 当然, 这些不同形貌 $BiVO_4$ 的内在形成机理还需进一步研究.

2.3 金属氧化态、氧物种和表面组成

图 3 为各 $BiVO_4$ 样品的 Bi 4*f*, V $2p_{3/2}$ 和 O 1*s* 的

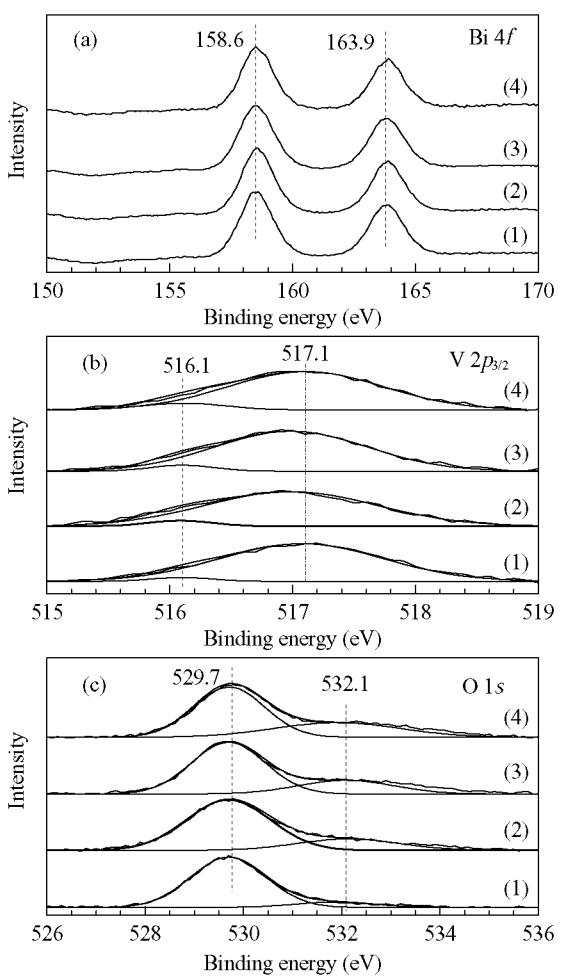

图 3 各 $BiVO_4$ 样品的 Bi 4*f*, V $2p_{3/2}$ 和 O 1*s* XPS 谱

Fig. 3. Bi 4*f* (a), V $2p_{3/2}$ (b), and O 1*s* (c) XPS spectra of $BiVO_4$-1 (1) $BiVO_4$-2 (2), $BiVO_4$-3 (3), and $BiVO_4$-4 (4).

XPS 谱. 可以看出, 所有 $BiVO_4$ 样品的 Bi 4*f* 谱在 E_b=158.6 和 163.9 eV 处出现两个明显的对称峰, 分别归属为 Bi $4f_{7/2}$ 和 Bi $4f_{5/2}$. 这意味着样品中 Bi 物种以 Bi^{3+}形式存在[30]. 由图 3(b) 可见, 各样品在 E_b=516.1 和 517.1 eV 处出现 V $2p_{3/2}$ 的不对称峰, 分别归属为 $V^{4+}BiVO_4$ 和 V^{5+}物种[31]. 这表明 $BiVO_4$ 样品中的 V 物种以 V^{4+} 和 V^{5+} 形式存在. 根据电中性原理, 可以推测到 $BiVO_4$ 样品存在氧空位 (即 $BiVO_{4-\delta}$), 表面非计量氧量 (δ) 取决于样品表面 V^{4+}/V^{5+}摩尔比. 再由图 3(c) 可见, 位于 E_b=530 eV 处的峰可以分解为 E_b=529.7 和 532.1 eV 两个峰, 分别归属为表面晶格氧 (O_{latt}) 和吸附氧 (O_{ads}) 物种[30]. 由于在 XPS 分析之前 $BiVO_4$ 样品已在 400 °C 的 O_2 气流中预处理过, 故样品表面上的 OH^-和 CO_3^{2-} 物种量很少. 因此, 氧吸附物种主要以 O^-, O_2^-或 O_2^{2-} 等形式存在, 且位于 $BiVO_{4-\delta}$中的氧空位上[32].

表 2 列出了 $BiVO_4$ 样品的表面 Bi/V, V^{4+}/V^{5+}和 O_{ads}/O_{latt}摩尔比. 可以看出, 每个样品的表面 Bi/V 摩尔比 (0.98~1.03) 都接近 1, 表明所制得的 $BiVO_4$ 很均匀. $BiVO_4$-4 表面 V^{4+}/V^{5+}摩尔比最高, 说明其含有最多的表面氧空位, 表面 O_{ads}/O_{latt}摩尔比也证实了这一点[32]. 氧空位的存在有利于提高 $BiVO_4$ 样品的光催化活性.

表 2 $BiVO_4$ 样品的表面 Bi/V, V^{4+}/V^{5+}和 O_{ads}/O_{latt}摩尔比

Table 2 Surface Bi/V, V^{4+}/V^{5+}, and O_{ads}/O_{latt} molar ratios of the $BiVO_4$ samples

Sample	Bi/V molar ratio	V^{4+}/V^{5+} molar ratio	O_{ads}/O_{latt} molar ratio
$BiVO_4$-1	0.99	0.037	0.115
$BiVO_4$-2	1.03	0.058	0.276
$BiVO_4$-3	0.98	0.061	0.345
$BiVO_4$-4	1.01	0.094	0.521

2.4 吸光性能

图 4(a) 为所得 $BiVO_4$ 样品的 UV-Vis 漫反射谱. 可以看出, 每个样品在紫外-可见光区均有明显的光吸收. 在可见光区的吸收是因带隙跃迁所致[33]. 这表明样品为单斜相 $BiVO_4$, 与 XRD 结果一致. E_g 大小可以反映晶型半导体的吸光性能. 可利用公式 $(\alpha h\nu)^2=A(h\nu-E_g)^n$ 计算, 其中 A, α 和 $h\nu$ 分别代表常数, 吸附系数和入射光能, n=1 时代表直接跃迁模式[10]. 每个 $BiVO_4$ 样品的 E_g 均根据 $(\alpha h\nu)^2$~$h\nu$ 曲线在 x 轴上的截距求得 (见图 4(b)). 所得 $BiVO_4$ 样品的 E_g 列于表 1 中. $BiVO_4$-1, $BiVO_4$-2, $BiVO_4$-3 和 $BiVO_4$-4 样品的 E_g 分别为 2.54, 2.52, 2.48 和 2.47 eV, 与文献[24,34]结果相当. 4 个样品中以 $BiVO_4$-4 样品的 E_g 最低, 表明其具有最好的可见光吸收性能, 因而在有机染料降解反应中应表现出更好的光催化活性.

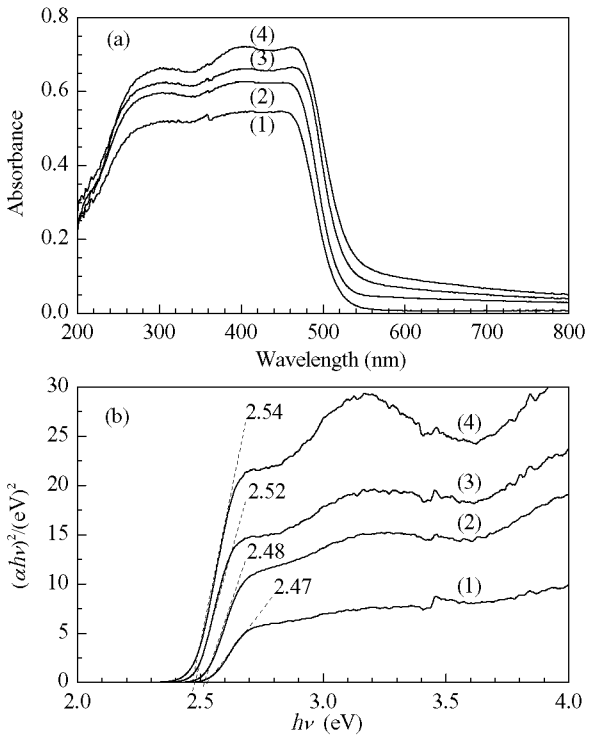

图 4 各 $BiVO_4$ 样品的 UV-Vis 漫反射谱和 $(\alpha h\nu)^2$ 随 $h\nu$ 的变化曲线

Fig. 4. UV-Vis diffuse reflectance spectra (a) and plots of $(\alpha h\nu)^2$ versus $h\nu$ of different $BiVO_4$ samples (b). (1) $BiVO_4$-1; (2) $BiVO_4$-2; (3) $BiVO_4$-3; (4) $BiVO_4$-4.

2.5 $BiVO_4$ 样品的光催化活性

图 5 为 Degussa P25 和 $BiVO_4$ 样品上光催化和直接光解降解 MO 反应的性能. 可以看出, 不加催化剂, 光照 4 h 后 MO 浓度仍无明显变化, 说明在该反应条件下 MO 很难被光解. 这与 Ge[19]的结果一致. 当以 P25 为催化剂时, 光照 4 h 后 MO 降解率约为 11%, 而各 $BiVO_4$ 样品的可见光催化活性更高, 其活性大小顺序为: $BiVO_4$-1 < $BiVO_4$-2 < $BiVO_4$-3 < $BiVO_4$-4, 反应 4 h 后 MO 转化率分别为 44%, 60%, 68% 和 87%, 好于文献[35]结果. 可以发现, 在这 4 个不同形貌的 $BiVO_4$ 样品中, 棒状 $BiVO_4$ 光催化降解 MO 能力明显更高.

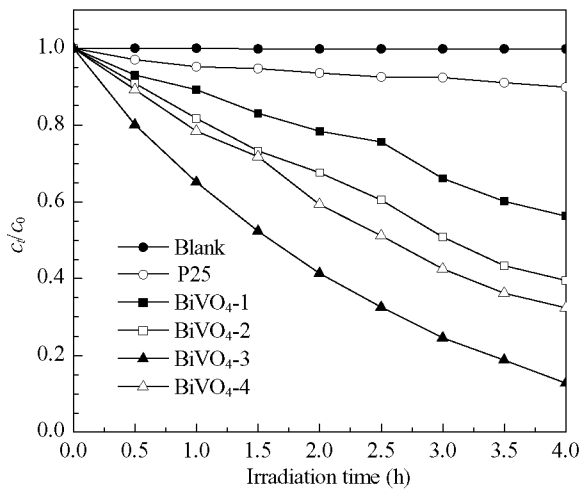

图 5 在可见光照射下直接光解, Degussa P25 和各 $BiVO_4$ 样品降解 MO 的光催化活性

Fig. 5. Photocatalytic activities of the blank (direct photolysis), Degussa P25, and $BiVO_4$-x (x = 1–4) samples for the degradation of MO under visible-light ($\lambda > 400$ nm) irradiation.

人们普遍认为, 晶相结构、结晶度和形貌是影响材料光催化性能的重要因素. 而本文所制得单斜相 $BiVO_4$ 样品都具有相似的结晶度. 因此, 这些 $BiVO_4$ 样品的光催化活性差异可能是形貌不同所致. 众所周知, 高表面能晶面的暴露率与材料的形貌有关, 因而形貌决定了此类材料的光催化性能. Mclaren 等[15]认为, ZnO 具有高表面能的晶面优先吸附 OH^- 离子, 有利于产生更多的 OH 自由基, 从而提高其光催化降解 MB 的活性. Wang 等[17]也发现, 层状 $BiVO_4$ 中具有更多 BiV_4 多原子中心的 (040) 晶面, 对改善其光催化释 O_2 的催化活性起到了决定性的作用. (040) 晶面暴露率的不同 (见图 1) 可能是不同形貌 $BiVO_4$ 样品的光催化活性不同的主要原因之一. 已有研究表明, 增大材料的比表面积有助于光致电子和空穴的分离, 从而提高其光催化活性[36]; 同时, 比表面积的增大和晶粒尺寸的减小有利于增强材料的光催化活性 (如 ZnO)[37]. 由前文可知, $BiVO_4$-4 样品粒子较小, 比表面积较大. 与其它 $BiVO_4$ 样品相比, 一方面, $BiVO_4$-4 样品具有最低的带隙能, 从而更有效地吸收可见光; 另一方面, 它具有较高的表面氧空位密度 (见表 2), 使其通过捕获更多的光致电子, 更有效地活化 O_2 分子, 从而抑制光致电子和空穴的复合[38,39]. 而且, $BiVO_4$ 样品形貌的不同导致其比表面积、表面氧空位密度和晶面暴露率的改变. 因此, 在 4 个 $BiVO_4$ 样品中, 棒状 $BiVO_4$-4 样品光催化活性最高. 综上所述, $BiVO_4$ 样品在光催化降解 MO 反应中存在形貌效应, 棒状 $BiVO_4$ 样品表现出最好的光催化活性.

3 结论

以硝酸铋和偏钒酸铵作金属源, 以 NaOH 调节 pH 值, 在有或无 P123 存在的条件下, 采用醇-水热法可以制得不同形貌的单斜白钨矿型 $BiVO_4$ 样品. 结果表明, 前驱体溶液的 pH 值和表面活性剂 P123 对所得 $BiVO_4$ 样品的粒子形貌有着显著影响. 在醇-水热温度 180 °C, pH = 2, 7 或 10 时, 可制得多孔球状、花状和片状 $BiVO_4$ 粒子; 当引入 P123 时, 在醇-水热温度 180 °C, pH = 2 时, 可制得棒状 $BiVO_4$ 粒子. 所得 4 种 $BiVO_4$ 样品的比表面积和带隙能分别为 1.4~3.8 m^2/g 和 2.47~2.54 eV. $BiVO_4$ 的粒子形貌不同使其比表面积、表面氧空位密度和 (040) 晶面暴露率也各不相同, 其中棒状 $BiVO_4$ 样品具有最高的比表面积、表面氧空位密度和 (040) 晶面暴露率以及最低的带隙能, 因而表现出最高的可见光催化降解 MO 的活性. 可以认为, $BiVO_4$ 材料的光催化活性存在形貌效应, 棒状形貌有利于提高 $BiVO_4$ 样品的光催化活性.

参 考 文 献

1 Lu T, Steele B C H. *Solid State Ionics*, 1986, **21**: 339
2 Hirota K, Komatsu G, Yamashita M, Takemura H, Yamaguchi O. *Mater Res Bull*, 1992, **27**: 823
3 Liu W, Yu Y Q, Cao L X, Su G, Liu X Y, Zhang L, Wang Y G. *J Hazard Mater*, 2010, **181**: 1102
4 Zhang X, Ai Z H, Jia F L, Zhang L Z, Fan X X, Zou Z G. *Mater Chem Phys*, 2007, **103**: 162
5 Tokunaga S, Kato H, Kudo A. *Chem Mater*, 2001, **13**: 4624
6 Sleight A W, Chen H Y, Ferretti A, Cox D E. *Mater Res Bull*, 1979, **14**: 1571
7 Yu J Q, Zhang Y, Kudo A. *J Solid State Chem*, 2009, **182**: 223
8 Neves M C, Trindade T. *Thin Solid Films*, 2002, **406**: 93
9 Sayama K, Nomura A, Zou Z G, Abe R, Abe Y, Arakawa H. *Chem Commun*, 2003: 2908
10 Zhou L, Wang W Z, Liu S W, Zhang L S, Xu H L, Zhu W. *J Mol Catal A*, 2006, **252**: 120
11 Yu J Q, Kudo A. *Adv Funct Mater*, 2006, **16**: 2163
12 Sun S M, Wang W Z, Zhou L, Xu H L. *Ind Eng Chem Res*, 2009, **48**: 1735
13 Zhang L, Chen D R, Jiao X L. *J Phys Chem B*, 2006, **110**: 2668
14 Li G R, Hu T, Pan G L, Yan T Y, Gao X P, Zhu H Y. *J Phys Chem C*, 2008, **112**: 11859

15 Mclaren A, Valdes-Solis T, Li G Q, Tsang S C. *J Am Chem Soc*, 2009, **131**: 12540
16 Xi G C, Ye J H. *Chem Commun*, 2010, **46**: 1893
17 Wang D E, Jiang H F, Zong X, Xu Q, Ma Y, Li G L, Li C. *Chem Eur J*, 2011, **17**: 1275
18 张妍, 于建强, 工藤昭彦, 赵修松. 催化学报 (Zhang Y, Yu J Q, Kudo A, Zhao X S. *Chin J Catal*), 2008, **29**: 624
19 Ge L. *Mater Chem Phys*, 2008, **107**: 465
20 索静, 柳丽芬, 杨凤林. 催化学报 (Suo J, Liu L F, Yang F L. *Chin J Catal*), 2009, **30**: 323
21 Meng X, Zhang L, Dai H X, Zhao Z X, Zhang R Z, Liu Y X. *Mater Chem Phys*, 2011, **125**: 59
22 Ke D N, Peng T Y, Ma L, Cai P, Dai K. *Inorg Chem*, 2009, **48**: 4685
23 Kudo A, Omori K, Kato H. *J Am Chem Soc*, 1999, **121**: 11459
24 Zhang A P, Zhang J Z, Cui N Y, Tie X Y, An Y W, Li L J. *J Mol Catal A*, 2009, **304**: 28
25 Li L Z, Yan B. *J Alloys Compd*, 2009, **476**: 624.
26 Zhou L, Wang W Z, Xu H L. *Cryst Growth Des*, 2008, **8**: 728
27 Xu A W, Antonietti M, Cölfen H, Fang Y P. *Adv Funct Mater*, 2006, **16**: 903
28 Chen L M, Liu Y N, Lu Z G, Zeng D M. *J Colloid Interface Sci*, 2006, **295**: 440
29 Gong Q, Qian X F, Ma X D, Zhu Z K. *Cryst Growth Des*, 2006, **6**: 1821
30 Xu H, Li H M, Wu C D, Chu J Y, Yan Y S, Shu H M, Gu Z. *J Hazard Mater*, 2008, **153**: 877
31 Liu W, Lai S Y, Dai H X, Wang S J, Sun H Z, Au C T. *Catal Lett*, 2007, **113**: 147
32 Yamazoe N, Teraoka Y, Seiyama T. *Chem Lett*, 1981: 1767
33 Zhang C, Zhu Y F. *Chem Mater*, 2005, **17**: 3537
34 Li H B, Liu G C, Duan X C. *Mater Chem Phys*, 2009, **115**: 9
35 Zhang A P, Zhang J Z. *Appl Surf Sci*, 2010, **256**: 3224
36 Yu J G, Xiong J F, Cheng B, Liu S W. *Appl Catal B*, 2005, **60**: 211
37 Mohajerani M S, Lak A, Simchi A. *J Alloys Compd*, 2009, **485**: 616
38 Lucky R A, Charpentier P A. *Appl Catal B*, 2010, **96**: 516
39 Wang Y X, Li X Y, Wang N, Quan X, Chen Y Y. *Sep Purif Technol*, 2008, **62**: 727

英 译 文
English Text

In recent years, bismuth vanadate has attracted considerable attention because of its unique physicochemical properties such as ferroelasticity [1], ion conductivity [2], and photocatalytic activity under visible-light irradiation [3,4]. Bismuth vanadate has three types of crystalline phases: tetragonal zircon, monoclinic scheelite, and tetragonal scheelite. $BiVO_4$ with a monoclinic scheelite structure gives far better visible-light-driven photocatalytic performance than those that have other crystal structures [5]. It is well known that the crystal structure of $BiVO_4$ is associated with the fabrication method. Tetragonal $BiVO_4$ is usually prepared by an aqueous precipitation route at low temperatures whereas monoclinic $BiVO_4$ can be obtained using various methods such as a solid-state reaction [6], co-precipitation [7], solvothermal or hydrothermal treatment [3,4], chemical bath deposition [8], organometallic decomposition [9], and sonochemical routes [10]. Among these strategies, the solvothermal or hydrothermal strategy is an effective pathway for the production of monoclinic $BiVO_4$ with perfect crystal structures and regular morphologies in an environmentally benign manner [11]. A large number of monoclinic $BiVO_4$ with different morphologies have been fabricated by the solvothermal or hydrothermal route, for example, monoclinically crystallized $BiVO_4$ with a spindly microtubular shape has been synthesized by solvothermally treating a mixture of $Bi(NO_3)_3$ and $NaVO_4$ in a deep eutectic solvent at 150 °C [3]. Sun and coworkers fabricated nanoplate-stacked star-like monoclinic $BiVO_4$ by a hydrothermal process with a water/ethanol mixture as the solvent and ethylenediamine tetraacetic acid as a chelating agent [12]. Using $Bi(NO_3)_3$ and NH_4VO_3 as starting materials and sodium dodecyl benzene sulfonate as a morphology-directing template, Zhang et al. [13] obtained monoclinic $BiVO_4$ nanosheets. Several reports have indicated that nano/microsized inorganic materials have morphology-dependent properties. For example, ZnO with various morphologies showed morphology-dependent catalytic activity and the ZnO material with large polar planes was more active in the *N*-formylation reaction [14]. Additionally, hexagonally plate-like ZnO nanocrystals along the (0001) axis gave about 5 times higher activity than rod-like ZnO particles while photocatalyzing the degradation of methylene blue [15]. Few reports exist that describe an investigation of the morphology-dependent properties of visible-light responsive $BiVO_4$. Xi et al. [16] observed good activities over the $BiVO_4$ nanoplates with exposed (001) facets for the visible-light photocatalytic degradation of rhodamine B (RhB) and for the photocatalytic oxidation of water for O_2 generation. Zhang et al. [13] observed good solar-light driven catalytic performance for $BiVO_4$ nanosheets with a preferred (010) surface orientation for the degradation of RhB. Li et al. [17] observed high activity over $BiVO_4$ microsheets with preferentially exposed (040) facets for the photocatalytic evolution of O_2 from water.

A large number of $BiVO_4$-based materials have been used as photocatalysts for the degradation of organics such as methylene blue (MB) [18], RhB [13], methyl orange (MO) [19], and toluene [20]. Recently, we investigated the controlled generation and photocatalytic applications of visi-

ble-light driven $BiVO_4$ single crystallites with well-defined morphologies and found that these morphological single crystalline materials performed well in the photocatalytic degradation of MB [21]. As an extension of this work, we report on the morphology-dependent photocatalytic behavior of monoclinic $BiVO_4$ with various particle shapes and these were fabricated by adopting the alcoho-hydrothermal strategy.

1 Experimental

1.1 Catalyst fabrication

$BiVO_4$ samples with different morphologies were fabricated using the alcoho-hydrothermal strategy with $Bi(NO_3)_3{\cdot}5H_2O$ and NH_4VO_3 as inorganic sources and a water/ethanol mixture as a solvent in the absence and presence of the triblock copolymer (P123) surfactant. The typical fabrication procedure was as follows: 10 mmol of well-ground $Bi(NO_3)_3{\cdot}5H_2O$ powder and 1.972 g of P123 (Bi/P123 molar ratio = 1:0.034) were added to a mixture of 5 ml of concentrated nitric acid (67%) and 50 ml of absolute ethanol under stirring. After mixing well, 10 mmol of well-ground NH_4VO_3 powder was added to the mixed solution. The pH was adjusted to 2, 7, or 10 with the saturated NaOH solution containing absolute ethanol. 80 ml of the mixture (a certain amount of absolute ethanol was added if the volume of the mixture was less than 80 ml) was then transferred to a 100 ml Teflon-lined stainless steel autoclave for alcoho-hydrothermal treatment at 180 °C for 12 h. The as-obtained yellow precipitate was filtered, washed three times with absolute ethanol, dried at 60 °C for 12 h and calcined in a muffle furnace at a ramp of 1 °C/min from room temperature (RT) to 400 °C and kept at this temperature for 4 h, thus generating the $BiVO_4$ sample. The samples fabricated under the various conditions are denoted $BiVO_4$-x (x = 1–4), as clearly described in Fig. 1.

1.2 Catalyst characterization

X-ray diffraction (XRD) patterns of the $BiVO_4$ samples were recorded on an X-ray diffractometer (Bruker D8 Advance), which was operated at 40 kV and 35 mA using Cu K_α radiation and a nickel filter (λ = 0.15406 nm). The surface areas of the samples were measured using an adsorption analyzer (Micromeritics ASAP 2020) by N_2 adsorption at −196 °C. The sample was degassed at 250 °C for 3 h before the measurement. The surface area was calculated using the Brunauer-Emmett-Teller (BET) method. The morphologies of the sample particles were observed using a scanning electron microscope (SEM, Gemini Zeiss Supra 55) operated at 10 kV. X-ray photoelectron spectroscopy (XPS, VG CLAM 4 MCD) was used to determine the Bi 4*f*, V 2*p*, and O 1*s* binding energies (E_b) of the surface bismuth, vanadium, and oxygen species. Mg K_α ($h\nu$ = 1253.6 eV) was used as the excitation source. Before the XPS measurement, the sample was treated in an O_2 flow of 20 ml/min at 400 °C for 1 h. After cooling to RT and using a glove bag (Instruments for Research and Industry, USA) filled with He, the pretreated sample was transferred to the spectrometer under He and outgassed (0.5 h) in the preparation chamber before analysis in the analysis chamber. The C 1*s* signal at 284.6 eV was used as a reference for E_b calibration. Ultraviolet-visible diffuse reflectance spectra (UV-Vis DRS) of the samples were recorded using a UV-Vis spectrophotometer (UV-2450) with $BaSO_4$ as the standard.

1.3 Catalyst evaluation

The photocatalytic activities of the $BiVO_4$ samples were evaluated for the degradation of MO in a quartz reactor (QO250, Beijing Changtuo Sci. & Technol. Co. Ltd.) under visible-light irradiation. A 300 W Xe lamp was used as the light source and was located about 5 cm from the reactor. An optical cut-off filter was used to only permit illumination at λ > 400 nm. 0.1 g of the $BiVO_4$ sample was added to 100 ml of the MO solution (initial MO concentration $c_0 = 1.0 \times 10^{-5}$ mol/L). After ultrasonication for 0.5 h, the solution was stirred magnetically for 3 h to allow the adsorption-desorption equilibrium to be reached. The temperature of the reaction solution was kept at ca. 25 °C using flowing cool water. Samples were taken at 30 min intervals and separated by centrifugation for MO concentration determination. The MO concentration (c_t) after a certain reaction time (t) was monitored by measuring the absorbance of the reactant solution at λ = 464 nm during the photodegradation process on the aforementioned UV-Vis equipment. The c_t/c_0 ratio was used to evaluate the photocatalytic degradation efficiency of the sample.

2 Results and discussion

2.1 Crystal phase and surface area

Figure 1 shows the XRD patterns of the $BiVO_4$ samples that were synthesized under various conditions. The diffraction peaks of all the samples could be well indexed to single-phase monoclinic $BiVO_4$ (JCPDS No. 83-1700), as indicated in Fig. 1(4). No impurity phases were detected. The slight discrepancy in peak intensity implies a similarity in the crystallinity of the $BiVO_4$ samples. This result indicates that a change in pH or the addition of P123 has an insignificant effect on the crystallinity of the $BiVO_4$ product. In other words, the calcination temperature plays an important role in

determining the crystallinity of the $BiVO_4$ sample. From Fig. 1, differences in the diffraction intensity of the (040) plane of these $BiVO_4$ samples are apparent. The XRD peak intensity ratio of the (040) plane to the (112) plane was found to be 0.22, 0.23, 0.32, and 0.36 for the $BiVO_4$-1, $BiVO_4$-2, $BiVO_4$-3, and $BiVO_4$-4 samples, respectively. A larger XRD peak intensity ratio indicates a higher percentage of exposed (040) planes for the $BiVO_4$ sample. It has been reported that the amount of exposed (040) planes in $BiVO_4$ is dependent upon the particle morphology and its fabrication procedure, and the preferential exposure of (040) planes can contribute to an enhancement in the photocatalytic activity of the $BiVO_4$ material [17].

Table 1 summarizes the fabrication conditions and some of the physical properties of the $BiVO_4$ samples. The $BiVO_4$-3 and $BiVO_4$-4 samples that were obtained after calcination at 400 °C possessed surface areas (3.5–3.8 m^2/g) much higher than the samples (0.3–2.2 m^2/g) obtained without calcination [22,23]. Additionally, the surface area (3.5 m^2/g) of $BiVO_4$-3 was higher than those (1.4–2.1 m^2/g) of $BiVO_4$-1 and $BiVO_4$-2. At a pH of 2, the P123-derived $BiVO_4$-4 sample had a far higher surface area (3.8 m^2/g) than the surfactant-free derived $BiVO_4$-1. These results indicate that the pH of the reactant solution and the surfactant P123 exerted a marked impact on surface area of the $BiVO_4$ sample. Similar phenomena are induced by the pH and surfactant as observed by Zhang et al. [24] and by our research group [22].

2.2 Morphology and formation mechanism

Figure 2 shows typical SEM images of the $BiVO_4$ samples. The $BiVO_4$-1 sample was composed of spherical microparticles with a porous structure and each spherical particle was aggregated into numerous cone-shaped microcrystals with diameters of 2–11 μm (Fig. 2(a) and (b)). By the homogeneous precipitation route and with the assistance of *N*,*N*-dimethylacetamide or *N*-methyl-2- pyrrolidone, Li et al. [25] generated submicrosized $BiVO_4$ with an irregular spherical morphology. With an increase in the pH from 2 to 7 or 10, the as-obtained $BiVO_4$-2 and $BiVO_4$-3 samples showed flower- and sheet-like morphology (Fig. 2(c–f)), respectively. $BiVO_4$ particles with a flower-like shape were also obtained by Ge [19]. With P123 as the surfactant and at a pH of 2, however, the as-obtained $BiVO_4$-4 sample had a rod-like architecture with a length of 0.5–3 μm and a diameter of 100–250 nm. These results indicate that the pH of the precursor solution and the surfactant has a significant influence on the morphology of the $BiVO_4$ material.

In the hydrothermal process the alkaline source, the metal precursor, the pH of the precursor solution, and the hydrothermal temperature and time greatly influence the morphology of the final product [26]. The formation of specifically morphological nano/microcrystals can be explained by the oriented aggregation mechanism [27]. In this mechanism, the primary particles self-assemble in preferential orientations into highly ordered superstructures with a well-defined external shape for the minimization of surface free energy. In this study, $BiVO_4$ particles with various morphologies might be generated according to the mentioned mechanism. Before the addition of the NaOH-ethanol solution, the precursor solution was highly acidic (pH = 0.8) and the vanadium species is mainly present as VO_3^- [28]. After the pH of the solution was adjusted to 1.5, the VO_3^- and BiO^+ generated in the precursor solution could interact to first form a number of $BiVO_4$ crystal nuclei, and then aggregate into primary nanoparticles. At pH = 2, 7, or 10, these primary nanoparticles could further self-assemble according to their specific orientations and finally crystallize into porous spherical, flower-like, or sheet-like $BiVO_4$ entities through Ostwald ripening and after calcination at 400 °C. For the P123-assisted fabrication, however, some of the surfactant molecules could selectively adsorb onto the surface of the $BiVO_4$ nuclei [29]. The adsorbed P123 molecules work as a capping agent and decrease the growth rate of the adsorbed crystal faces while inducing compression along the axis perpendicular to these facets, thus forming $BiVO_4$ nano/microrods. However, the inherent formation mechanism needs further investigation.

2.3 Metal oxidation state, oxygen species, and surface composition

Figure 3 shows the Bi 4*f*, V $2p_{3/2}$, and O 1*s* XPS spectra of the $BiVO_4$ samples. From Fig. 3(a), the Bi 4*f* spectra of all of the $BiVO_4$ samples consist of two strong symmetrical peaks at E_b = 158.6 and 163.9 eV, corresponding to the Bi $4f_{7/2}$ and Bi $4f_{5/2}$ signals, respectively. These spectra are characteristic of the Bi^{3+} species [30]. In other words, all the bismuth in the $BiVO_4$ samples are trivalent [30]. From Fig 3(b), the asymmetric V $2p_{3/2}$ signal was decomposed into two peaks at E_b = 516.1 and 517.1 eV, attributable to the surface V^{4+} and V^{5+} species [31], respectively. This result indicates the co-presence of V^{5+} (in the majority) and V^{4+} (in the minority) species in the $BiVO_4$ samples. Based on the electroneutrality principle, one can deduce that the $BiVO_4$ samples were oxygen-deficient (i.e., $BiVO_{4-\delta}$) and the amount of surface nonstoichiometric oxygen (δ) is dependent upon the surface V^{4+}/V^{5+} molar ratios. As for the O 1*s* XPS spectra (Fig. 3(c)), the asymmetric peak centered at ca. 530 eV was decomposed into two components at E_b = 529.7 and 532.1 eV, and these are due to the surface lattice oxygen (O_{latt}) and the adsorbed oxygen (O_{ads}) species, respectively [30]. Since the $BiVO_4$ samples were pretreated in an O_2 flow at 400 °C before the XPS analysis, the presence of surface OH^- and CO_3^{2-} species

on the sample surfaces could be minimized. Therefore, the adsorbed oxygen species were mainly O^-, O_2^-, or O_2^{2-} species, which were located at the oxygen vacancies of the $BiVO_{4-\delta}$ samples [32].

The surface Bi/V, V^{4+}/V^{5+}, and the O_{ads}/O_{latt} molar ratios of the $BiVO_4$ samples are summarized in Table 2. The surface Bi/V molar ratio (0.98–1.03) of each $BiVO_4$ sample was close to 1, and this is indicative of homogeneous $BiVO_4$ phase formation. The highest surface V^{4+}/V^{5+} molar ratio for the $BiVO_4$-4 sample suggests that it contains the highest amount of surface oxygen vacancies, and this was confirmed by the O_{ads}/O_{latt} molar ratio of this sample because the O_{ads} species were mainly located at the surface oxygen vacancies [32]. The presence of oxygen vacancies may be advantageous for the enhancement in photocatalytic performance of the $BiVO_4$ material.

2.4 Light absorption property

Figure 4(a) shows the UV-Vis diffuse reflectance spectra of the $BiVO_4$ samples. All the samples showed a strong absorption in the UV- and visible-light regions, and visible-light absorption was due to the bandgap transition [33]. These absorption profiles suggest the generation of monoclinic $BiVO_4$ in the samples, as substantiated by XRD results (Fig. 1). The bandgap energy (E_g) can be used to evaluate the optical absorption performance of a crystalline semiconductor according to the equation: $(\alpha h\nu)^2 = A(h\nu - E_g)^n$, where A, α, and $h\nu$ are a constant, the absorption coefficient, and the incident photon energy, respectively, while n is 1 for a direct transition [10]. The E_g of each $BiVO_4$ sample was obtained from the intercepts of the $(\alpha h\nu)^2$ versus photon energy ($h\nu$) plots, as shown in Fig. 4(b). The E_g values of the $BiVO_4$ samples are summarized in Table 1. The E_g was 2.54, 2.52, 2.48, and 2.47 eV for the $BiVO_4$-1, $BiVO_4$-2, $BiVO_4$-3, and $BiVO_4$-4 samples, respectively. The E_g values of these $BiVO_4$ samples were comparable to those (2.39–2.51 eV) of the $BiVO_4$ materials reported in the literature [24,34]. Compared with the other $BiVO_4$ samples, $BiVO_4$-4 had the lowest E_g value, indicating that the latter was more effective in absorbing visible light and would hence exhibit better photocatalytic performance for the degradation of organic dyes under visible-light irradiation, as confirmed by the photocatalytic activity data below.

2.5 Photocatalytic performance

The photocatalytic activities of the $BiVO_4$ samples were measured for the degradation of MO in an aqueous solution under visible-light irradiation. For comparison purposes, the MO direct photolysis (blank experiment) and MO degradation over commercial TiO_2 (Degussa P25) nanoparticles under identical conditions were also conducted. Figure 5 shows the MO concentration ratios (c_t/c_0) of the different samples as well as that of the direct photolysis process with irradiation time. Apparently, the MO concentration in the blank experiment showed no obvious change after visible-light irradiation over 4 h, indicating that MO was hardly photolyzed under these conditions. Similar phenomena were also observed by Ge [19]. Over the P25 sample, the MO conversion after 4 h of visible-light irradiation was ca. 11%. The $BiVO_4$ samples, however, exhibited much better visible-light-driven photocatalytic performance than the P25 sample, and the MO conversion increased as follows: $BiVO_4$-1 < $BiVO_4$-2 < $BiVO_4$-3 < $BiVO_4$-4. For the 4 h reactions, the MO conversion was ca. 44%, 60%, 68%, and 87% over the $BiVO_4$-1, $BiVO_4$-2, $BiVO_4$-3 and $BiVO_4$-4 samples, respectively. This photocatalytic performance was far better than that (20% within 4 h of reaction) obtained over the $BiVO_4$ material reported elsewhere [35]. Among the four $BiVO_4$ samples with different morphologies, the rod-like morphology was significantly better than the other morphologies in photocatalyzing the degradation of MO.

It has been generally accepted that the crystal structure, crystallinity and morphology of a material are important factors that influence its photocatalytic performance. As revealed by XRD, all the $BiVO_4$ samples have a monoclinic crystal structure with similar crystallinity. The discrepancy in photocatalytic activity of these $BiVO_4$ samples is not due to the crystal structure and crystallinity. Therefore, the morphology might be the main factor that influences the photocatalytic property of the monoclinically crystallized $BiVO_4$ materials. The percentage of exposed crystal planes with high surface energy is related to the morphology of a material, which determines its photocatalytic performance. For example, Mclaren et al. [15] claimed that crystal planes with a high ZnO surface energy preferred to adsorb OH^- ions, which could result in a higher OH radical production rate and hence facilitate the degradation of MB during the photocatalytic process. Wang et al. [17] indicated that (040) crystal planes with more BiV_4 multi-atomic centers consisting of $BiVO_4$ sheets plays a decisive role in enhancing the photocatalytic activity for the evolution of O_2. The difference in (040) plane exposure (Fig. 1) might make a partial contribution to the discrepancy in photocatalytic performance of the $BiVO_4$ samples. Previous studies have shown that (i) the rise in surface area can enhance the photocatalytic performance of a material because of the promotional effect of the electron-hole separation [36], and (ii) the increase in surface area and the decrease in crystalline grains are beneficial for the enhancement in photocatalytic activity of a material (e.g., ZnO) [37]. Our SEM and BET results show that the $BiVO_4$-4 sample has a smaller particle size and a higher surface area than the other $BiVO_4$ samples. Compared with the other

$BiVO_4$ samples, the $BiVO_4$-4 sample had the lowest E_g and this gives rise to the most effective absorption of visible light. On the other hand, the $BiVO_4$-4 sample exhibited a higher surface oxygen vacancy density (Table 2), which allows it to activate oxygen molecules more effectively by capturing more photoelectrons and thus greatly inhibiting their recombination with photoinduced holes [38,39]. Furthermore, the difference in morphology results in different surface areas, surface oxygen vacancy densities, and (040) crystal plane exposure for $BiVO_4$. Therefore, it is understandable that the rod-like $BiVO_4$-4 sample performed the best among the four $BiVO_4$ samples. Based on the above results and discussion, we conclude that a morphological effect is responsible for the photocatalytic performance and the rod-like morphology favors an increase in the photocatalytic performance of the $BiVO_4$ material.

3 Conclusions

Monoclinic scheelite-type $BiVO_4$ samples with various morphologies were produced using a facile alcoho-hydrothermal strategy with bismuth nitrate and ammonium metavanadate as the metal sources and NaOH as a pH adjustor in the absence or presence of P123. We found that the pH of the precursor solution and the P123 surfactant strongly influences the particle morphology and structure of the $BiVO_4$ sample. Porous spherical, flower-like, and sheet-like $BiVO_4$ particles were generated with the addition of P123 at an alcoho-hydrothermal temperature of 180 °C and at a pH of 2, 7, or 10, respectively. At an alcoho-hydrothermal temperature of 180 °C and at a pH of 2, a rod-like $BiVO_4$ material was obtained. The surface areas and bandgap energies of the four $BiVO_4$ samples ranged from 1.4–3.8 m^2/g and 2.47–2.54 eV, respectively. The difference in morphology of the $BiVO_4$ particles results in differences in the surface area, the surface oxygen vacancy density and the (040) crystal plane exposure. The rod-like $BiVO_4$ sample with the highest surface area, surface oxygen vacancy density and (040) crystal plane exposure, and the lowest bandgap energy gave the best photocatalytic performance for the degradation of MO under visible-light illumination. We conclude that the photocatalytic activity of the $BiVO_4$ material is affected by its morphology and the rod-like morphology favors an increase in the photocatalytic performance.

Full-text paper available online at Elsevier ScienceDirect
http://www.sciencedirect.com/science/journal/18722067